# Multi-scale variability of internal solitary wave speed in the Sulu Sea

**Xixi Li[1,3,5], Jianjun Liang[2,1,3], Kaiguo Fan[4] and Xiao-Ming Li[2,1,3]**

[1]Key Laboratory of Digital Earth Science, Aerospace Information Research Institute, Chinese Academy of Sciences, Beijing, 100094, China.

[2]Key Laboratory of Earth Observation of Hainan Province, Hainan Aerospace Information Research Institute, Wenchang, 571333, China.

[3]International Research Center of Big Earth Data for Sustainable Development Goals, Beijing, 100094, China.

[4]School of Meteorology and Oceanography, National University of Defense Technology, Changsha 410015, China

[5]University of Chinese Academy of Sciences, Beijing, 100049, China.

Corresponding authors: Xiao-Ming Li and Jianjun Liang (lixm@radi.ac.cn, liangjj@radi.ac.cn)

**Key Points:**

- Satellite observations yield wave speeds of ISWs in the Sulu Sea presenting multi-scale temporal variations from days to years.
- Tidal currents and seasonal circulations significantly modulate the wave speed.
- Evidence for interannual variation of wave speed driven by ENSO is presented.

## Abstract

Internal solitary waves (ISWs) have considerable energy to drive the mixing of water masses in the Sulu Sea. The propagation speed is a critical parameter in demonstrating the dynamic characteristics of ISWs. We collected 1354 groups of ISWs' speeds from tandem satellite remote sensing images with short temporal intervals and analyzed their spatial and multi-scale temporal variations in the Sulu Sea. The wave speeds increase exponentially with water depth with a power of 0.26. The fortnightly spring/neap tidal currents cause daily variations of wave speeds up to 30%. In addition to the well-recognized stratification that leads to monthly variations of wave speed, the seasonal circulations lead to a maximum decrease of wave speeds by 0.27 m/s. With respect to interannual variations, the wave speeds increase in La Niña years and decrease in El Niño years, caused by the climatic modulation of ocean stratification.



## Plain Language Summary

Internal solitary waves (ISWs) are a subsurface analogy of surface gravity waves. They are characterized by large vertical isopycnal displacements and strong current shears. Understanding their characteristics and variations is essential to know how they generate and dissipate. The Sulu Sea, which has high-frequency and strong ISWs, is a natural laboratory for exploring the secrets of ISWs. The propagation speed is one of the critical parameters in studying the characteristics of the dynamical processes of ISWs. In this paper, we collected 1354 groups of ISWs' speeds in the Sulu Sea using tandem satellite images and analyzed their spatiotemporal variations. The results reveal that the variations of ISWs' speeds are primarily dependant on water depth, ocean stratification and background currents. Above all, it is the first time to give observational evidence about the appreciable effect of tidal currents, seasonal circulations, and El Niño Southern Oscillation on ISWs' speeds from days through months to years.


## 1 Introduction

Internal solitary waves (ISWs) are ubiquitous oceanic dynamics, characterized by a temporal scale of tens of minutes and a spatial scale of hundreds to thousands of meters (Zheng and Klemas, 1993; Apel, 2002; Jackson, 2004). They present an indispensable step for the energy cascade from barotropic tides to diapycnal mixing (Garrett, 2003; Mackinnon et al., 2017). Moreover, ISWs greatly affect acoustic propagation (Zhou et al., 1991; Apel et al., 2007; Lynch et al., 2010), submarine navigation (Osborne et al., 1978; Wang et al., 2022), nutrient distribution (Haury et al., 1979; Wang et al., 2007), and sediment transport (Da Silva, 2002). Understanding their characteristics, variability, formation, and fate is important to parameterize their mixing in numerical climate models (Alford et al., 2015).

Sulu Sea (SS, Figure 1a) is a natural laboratory to study the characteristics and dynamic processes of ISWs (Apel et al., 1985; Liu et al., 1985; Liu et al., 2019). The ISWs in the SS are thought to be generated by the lee-wave mechanism (Apel et al., 1985). The ebb tide traps a thermocline depression; then, as the tide turns, the depression escapes upstream over the sill barrier. They are formed near the Pearl Bank sill and propagate through the basin to dissipate as they reach Palawan Island (Apel et al., 1985; Jackson et al., 2011). During their lifetime in the SS, complex factors can affect the ISWs' generation and evolution: the fortnightly spring/neap tidal cycle, seasonal circulations in the upper layer (Cai et al., 2009; Han et al., 2009), and the

climate effect related to the El Niño–Southern Oscillation (ENSO) (Klein et al., 1999). However, how these factors affect the dynamic processes of ISWs in the SS is still poorly understood.

Propagation speed is one of the critical parameters to understanding dynamics and energetics of the ISWs (Jackson et al., 2009; Lien et al., 2012; Zhang et al., 2022), also called wave speed (Liu et al., 1985). Many studies have tried to figure out the characteristics and variations of wave speed. By deploying moorings along a wave propagation path, researchers estimate wave speed according to the wave arrival times at nearby moorings (Ramp et al., 2010; Huang et al., 2017). However, field experiments are often costly and may introduce uncertainties due to the considerable distance between mooring sites. Since the launch of the SEASAT in 1978, satellite remote sensing has been proven to be a powerful tool in investigating ISWs (Alpers et al., 1985; Da Silva et al., 1998; Jackson et al., 2007). With the advantage of large spatial coverage and high temporal resolution, satellite images are widely used for estimating wave speed. In the early days, the wave speed was roughly calculated with a single satellite image containing two wave packets separated by one tidal period (Porter and Thompson, 1999; Li et al., 2000; Liu et al., 2004). Later, the emergence of multi-source and multi-type satellites provides conditions for using tandem satellite images to calculate the wave speed (Liu et al., 2014).

Based on satellite observations and field measurements, many studies show that wave speed is primarily dependent on water depth (Jackson et al., 2009; Liu et al., 2014; Lindsey et al., 2018; Liu et al., 2019; Tensuban et al., 2021) and has seasonal variations mainly controlled by ocean stratification (Gises et al., 1998; Liu et al., 2014; Cho et al., 2016; Liu et al., 2019). However, in this study, we found that the wave speed in the SS is also strongly modulated by tidal currents, seasonal circulations, and ENSO. Thus, the wave speed in the SS exhibits a multi-scale temporal variation, from daily through monthly to interannual variation due to the abovementioned environmental factors.

Here, we show such a multi-scale variation of wave speed by in the SS by collecting 1354 groups of wave speeds using tandem satellite images with temporal intervals typically shorter than 20 minutes. The details of the data and method are described in Section 2. Section 3 presents the spatial and multi-scale temporal variations of the wave speeds. Discussion and conclusions are in Section 4.

## 2 Data and Methods

### 2.1 Satellite images

This study uses satellite images taken by Moderate Resolution Imaging Spectroradiometer (MODIS) onboard Aqua and Visible Infrared Imaging Radiometer Suite (VIIRS) onboard Suomi National Polar-orbiting Partnership (NPP) satellites. The former has a swath of 2330 km and the latter has an even wider swath of 3060 km. The MODIS and VIIRS data have a spatial resolution of 250 m and 375 m, respectively. Large swath coverage and moderate spatial resolution of the two sensors are particularly effective in tracking ISWs with spatial scales of thousands of meters in the SS. Combining the two sensors additionally yields short temporal intervals of observations for accurate estimation of wave speeds. Finally, we collected 41 image pairs acquired by NPP/VIIRS and AQUA/MODIS (called NPP-AQUA pair hereafter) from 2015 to 2022 with temporal intervals ranging from 5 to 19 minutes.

### 2.2 ISW speeds estimated from tandem satellite images

The MODIS and VIIRS data are projected into GCS_WGS_1984 geographic coordinate system. We draw a line normal (white arrows in Figure 1b) to the two dark strips of the same ISW observed by two satellites (red and blue lines) and then measured the length of the normal line. The wave speed was calculated by dividing the spatial displacement of the ISW by the temporal interval of the two satellite images. In total, 1354 groups of wave speeds were obtained, and their spatial distribution is shown in Figure 1a.

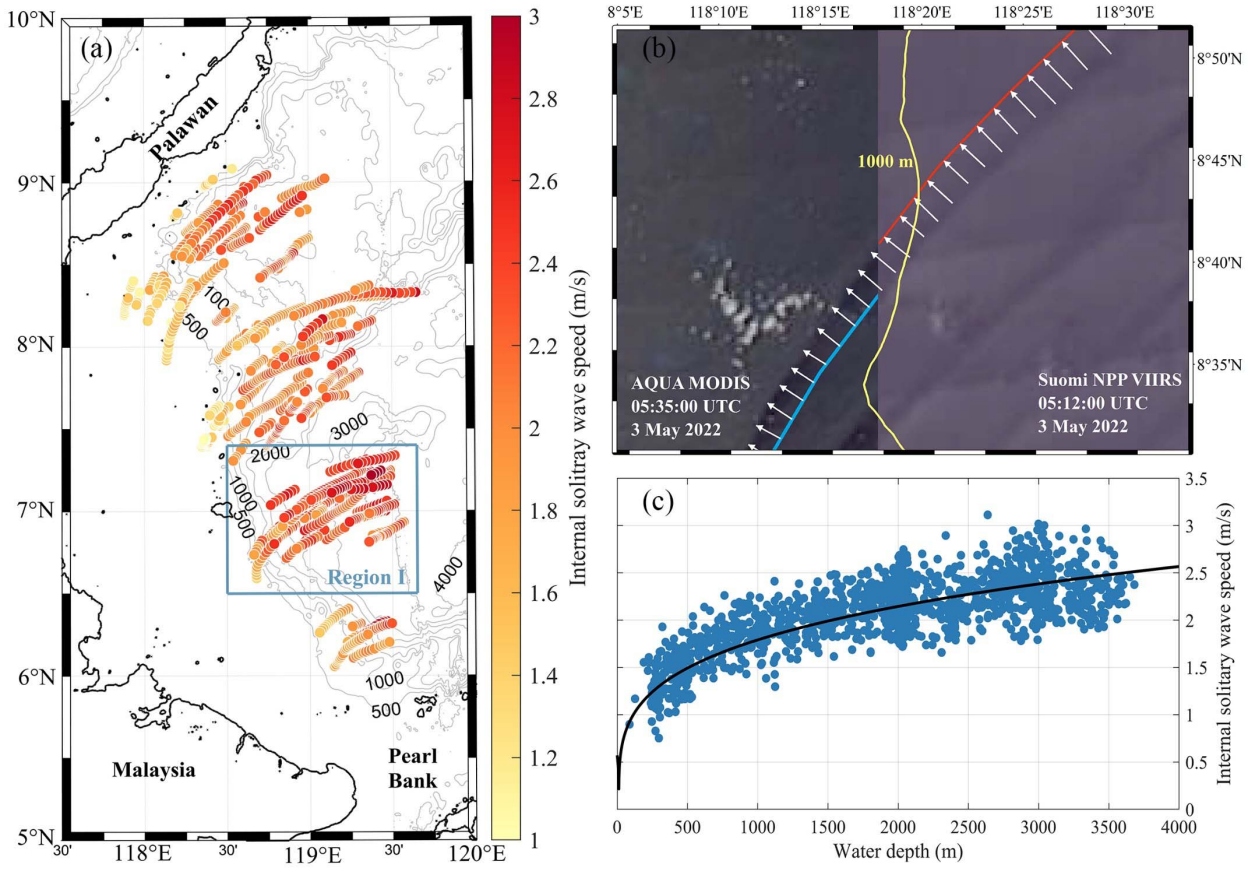


**Figure 1.** (a) The spatial variation of the wave speeds in the Sulu Sea. Each dot represents a displacement of ISW and its color means the magnitude of wave speed. The gray line is the isobath and the black line is the coastline. The blue solid rectangles show the study region for Section 3.2. (b) presents an NPP-AQUA pair of images acquired on 3 May 2022. The red and blue lines are the wave crests in the MODIS and VIIRS images, respectively. White arrows represent the displacements of the ISW.The yellow line represents 1000 m isobath. (c) shows the variation of wave speed with water depth. The black line represents the fitting curve.

### 2.3 Linear phase speeds derived from the Sturm-Liouville equation

The phase speed of a linear internal wave can be determined by solving the Sturm-Liouville (S-L) equation (Gill, 1982)

$$\frac{d}{dz}\left[(U_B(z)-c_0)^2\frac{d\varphi}{dz}\right]+N^2\varphi=0 \qquad (1)$$

subject to the boundary conditions:

$$\varphi(0) = \varphi(-H) = 0 \tag{2}$$

where $\varphi$ and $c_0$ represent the vertical structure and linear phase speed, respectively. $U_B(\mathrm{z})$ is the background current velocity. $N^2$ is the squared buoyancy frequency relating to the stratification. $H$ is water depth. Information about bathymetry, ocean stratification, and background currents are all needed to solve equation (1). We obtained the local bathymetry in 15 arc-second interval grids from GEBCO_2022 datasets (GEBCO Compilation Group, 2022). The Hybrid Coordinate Ocean Model (HYCOM) run at 1/12° resolution provides information about ocean stratification and background current (Chassignet et al., 2007). Argo profiling data in 2007, 2008, 2009, and 2015 to 2019 are used to obtain actual ocean stratification data (see details in S1).

In a two-layer ocean model, $c_0$ can be calculated by

$$c_0 = \sqrt{\frac{g\sigma h_1 h_2}{h_1 + h_2}} \tag{3}$$

where $h_1$ and $h_2$ are the upper and lower depths, respectively. $g$ is the gravitational acceleration, $\sigma = 2(\rho_2 - \rho_1)/(\rho_2 + \rho_1)$ is the relative layer density difference, and $\rho_1(\rho_2)$ is the density of the upper (lower) layer.

ISWs are nonlinear waves, and thus their wave speed $c$ is not equal to the linear phase speed $c_0$. According to the Korteweg-de Vries (KdV) theory, the two speeds are related by the following equation:

$$c = c_0 + \frac{\alpha\eta_0}{3} \tag{4}$$

where $\eta_0$ is the wave amplitude and α is the nonlinear coefficient. Equation 4 predicts that wave speed consistently exceeds linear phase speed because the productive of α and $\eta_0$ is positive.

## 3 Spatiotemporal characteristics of ISW speed

### 3.1 Spatial variation

As shown in Figure 1a, the wave speeds roughly increase from the shallow Pearl Bank (5.87°N, 119.8°E), peak at the place near 7°N (the marked Region I), and then gradually decrease towards Palawan Island. For a single ISW, its speed decreases from east to west, corresponding to a decreasing water depth. For example, in Figure 1b, the ISW acquired on 3 May 2022 has a higher average speed (2.32 m/s) on the east side of the 1000 m isobath than on its west side (1.71 m/s). Thus, the bathymetry in the SS has a significant impact on the spatial variation of wave speeds. We derived the relationship between the wave speeds ($c$) and water depth ($H$), as presented by the fitting curve (black line) in Figure 1c. The fitting formula is:

$$c = 0.421 \times (0.274 \times H + 0.647)^{0.261} \tag{5}$$

The formula suggests that the wave speeds increase exponentially with water depth with a power of 0.26, indicating that the water depth significantly modulates the wave speeds. Thus, this strong bathemetry effect may interfere with our study of the impacts of tidal currents, ocean stratification, and background currents on wave speeds.To reduce this interference, here, we define $H_0$ = 500 m as the threshold (see details in S2), beyond which the the effect of bathymetry can be neglected.

In addition, Figure 1c demonstrates that wave speeds vary considerably for the same water depth, suggesting the temporal variations and manual error in estimating wave speeds from satellite images. Statistically, based on a large amount of data, the manual error will not influence the following analysis about the temporal variations of wave speeds.

### 3.2 Daily variation

According to equation 4, tidal currents may influence the wave speed by changing the wave amplitude $\eta_0$ (Apel et al., 1985). To explore the effect of tidal currents, we delineated Region I (see details in S3) as the study area where wave speeds from 16 ISWs were extracted. We compared these wave speeds and their linear counterparts with the maximum ebb tidal current speeds corresponding to the wave generation. The dark-red dots in Figure 2a are the satellite-derived wave speeds, which reveals that they increase by 31% when the maximum ebb current speeds increase from 50 cm/s to 91 cm/s. The fitting function is:

$$c = 8.85 \times 10^{-5} \times {U_{wavemax}}^2 + 2.055 \quad (6)$$

where $U_{wavemax}$ represents the maximum ebb tidal current speed predicted by the barotropic tidal models. Here we use the regional TPXO tidal solutions in the Indian Ocean (Egbert and Erofeeva, 2002). The estimation of $U_{wavemax}$ is described in the S4. It is the first time to show how the tidal currents quantitively affect the wave speeds (Equation 6).

The strong tidal current creates ISWs with large amplitude (Wang et al., 2011); the larger the amplitude, the greater the nonlinear part of the wave speeds ($\alpha\eta_0/3$ in equation 4). However, the linear phase speed (the dark-blue dots in Figure 2a) is independent of wave amplitude and varies with ocean stratification and background currents. The speeds used here are all acquired in April, May and June (called AMJ month hereafter, seeing details in S3). Thus, ocean stratification and background currents (dominated by monsoon) have small change, and so do the linear phase speeds.

Figure 2b presents the $U_{wavemax}$ and the corresponding wave speeds estimated from equation 6 in a typical spring/neap tidal cycle, showing synchronized changes in the $U_{wavemax}$ and wave speeds on a daily scale. The wave speeds increase by 30% from the neap to spring tide period, indicating that tidal currents significantly impact the daily variation of the wave speeds.

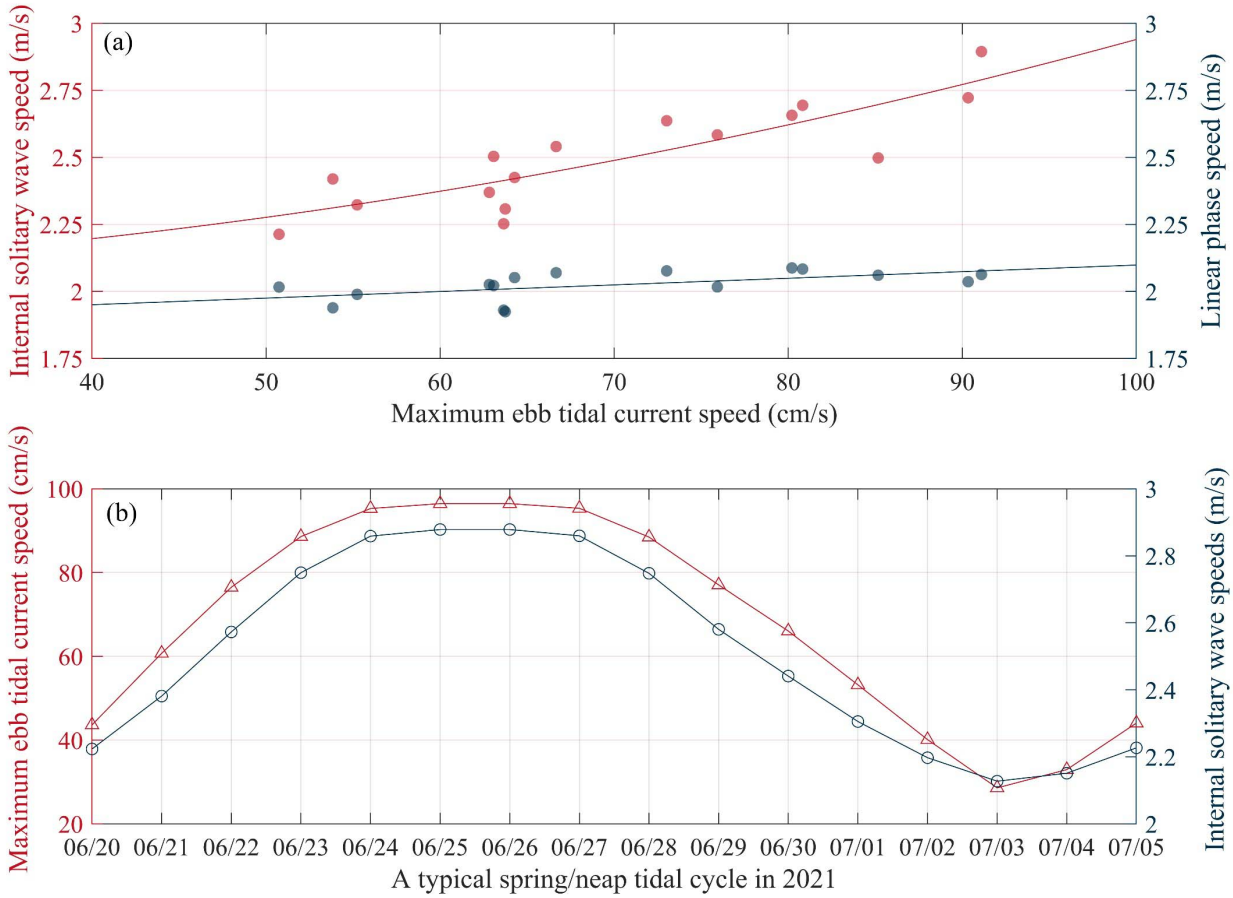


**Figure 2.** (a) The relationship between the satellite-derived speeds (red dots) and their linear phase speeds (dark-blue dots) with the maximum ebb tidal current speeds. The lines with different colors represent the fitting curve for the corresponding scatterd dots. (b) The maximum ebb tidal currents (red triangles) and the corresponding wave speeds (dark-blue circles)in a typical spring/neap tidal cycle from 20 June 2021 to 5 July 2021.

### 3.3 Monthly variation

In this section, 1231 groups of wave speeds (see details in S3) were used to study their monthly variation ($c$ in Figure 3a). The wave speed decreases from January to February, and then fluctuates up until August. After that, it rapidly drops to the lowest value in October and then maintains its upward trend until December.

Ocean stratification is a recognized factor that impacts the monthly wave speed variation. To analyze the effects of stratification on wave speeds, we collected profiling data from all Argo floats in the SS to derive monthly averages of the maximum value of buoyancy frequency ($N_{max}$) and the depth at $N_{max}$ ($N_{maxdepth}$), which are shown in Figure 3b and 3c, respectively. It is worth noting that the ISWs were not detected in tandem satellite images in July during 2015 to 2022, therefore, the $N_{max}$ and $N_{maxdepth}$ in July are also excluded in comparsion. From Figure 3a to 3c, we found that $N_{max}$ ($N_{maxdepth}$) reaches its highest (lowest) in August, while the corresponding wave speed is also the largest in August. This result can be explained by

equation 3: higher $N_{max}$ and lower $N_{maxdepth}$ imply larger $\sigma$ and higher $h_1$, and thus higher linear phase speed of ISW, suggesting the enhanced ocean stratification increases wave speeds.

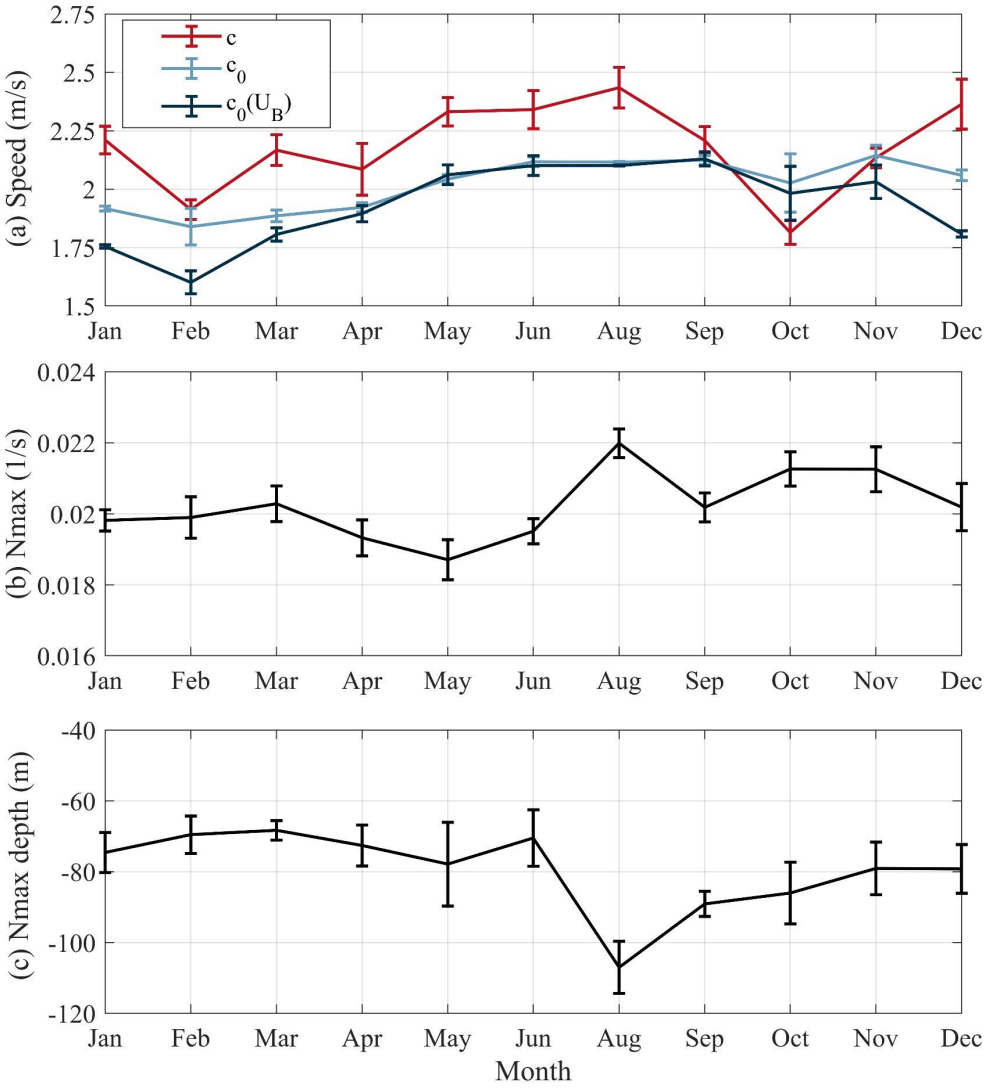


**Figure 3.** (a) The monthly variations of satellite-derived wave speeds ($c$), HYCOM-derived linear phase speeds without ($c_0$) and with ($c_0(U_B)$) background currents. (b) and (c) presents the monthly variation of $N_{max}$ and $N_{maxdepth}$ estimated from Argo profiling data, respectively. The vertical bars represent ranges of one standard deviation.

Previous studies show a basin-scale anticyclonic/cyclonic circulation in the upper layer of SS caused by the summer/winter monsoon (Cai et al., 2009; Han et al., 2009). This unique feature may also play a role in modulating the monthly variation of wave speeds. Here, we used the HYCOM datasets to estimate the corresponding linear phase speeds of the satellite-derived wave speeds ($c$) through equation 1 without ($c_0$) and with ($c_0(U_B)$) background currents ($U_B(z)$ in equation 1). The monthly variations of $c$, $c_0$, and $c_0(U_B)$ in Figure 3a show that the background currents do modulate the wave speeds, especially from October to March with

differences up to 0.27 m/s between $c_0$ and $c_0(U_B)$, indicating that the background currents impact the monthly variation of the wave speeds.

There are some other interesting findings in Figure 3a. In October and November, the $c_0$ are higher than $c$, contrary to the KdV theory (equation 4). After superimposing the background currents, the result in November is consistent with the KdV theory, but the result in October still challenges it. The reason for this condradiction may be a flaw in the KdV theory or the uncertainty of the model-derived stratification for calculating phase speeds.

### 3.4 Interannual variation

On interannual scales, the ENSO affects the stratification of the SS by changing precipitations and sea surface temperature. Generally, the stratification is strengthened in La Niña years and weakened in El Niño years (DeCarlo et al., 2015; Emberson et al., 2021). The occurrence of La Niña and El Niño years can be diagnosed by the NINO3.4 index of ENSO (Trenberth and Stepaniak, 2001). To investigate the effect of ENSO on wave speed, we collected all available Argo profiling data in the SS for estimating the $N_{max}$ and $N_{maxdepth}$. Figure 4a, 4b and 4c show the interannual variations of $N_{max}$, $N_{maxdepth}$, and the NINO3.4 index, respectively. The $N_{max}$ increases and the $N_{maxdepth}$ decreases with the decrease of the NINO3.4 index. 2015 was a strong El Niño year, in which the $N_{max}$ reaches its lowest value among the eight years and $N_{maxdepth}$ also becomes shallow. The Pearson correlation coefficients are -0.46 (the NINO3.4 index and $N_{max}$) and 0.68 (the NINO3.4 index and $N_{maxdepth}$), suggesting that stratification was enhanced with the decrease of the NINO3.4 index. Besides, according to Section 3.3, greater $N_{max}$ and smaller $N_{maxdepth}$ imply greater $c_0$, indicating that there is a negative correlation between wave speed and NINO3.4 index.

We collected 759 wave speeds from 46 ISWs to examine our analysis of the impact of ENSO on wave speeds (see details in S3). The comparison between wave speed and the NINO3.4 index from 2016 and 2022 (no ISW was detected in tandem satellite images in the AMJ month of 2015) is made with the following cautions: the NINO3.4 index used here is the average of AMJ month for each year to ensure the consistency of data during comparison since the wave speeds are only collected in the AMJ month.

The interannual variations of wave speeds (Figure 4d) and the NINO3.4 index (Figure 4e) are presented. Their Pearson correlation coefficient is -0.79, suggesting that there is a strong year-to-year inverse correlation between wave speed and the NINO3.4 index. In specific, the wave speed increases in La Niña years and decreases in El Niño years, in agreement with our theoretical analysis based on the Argo data.

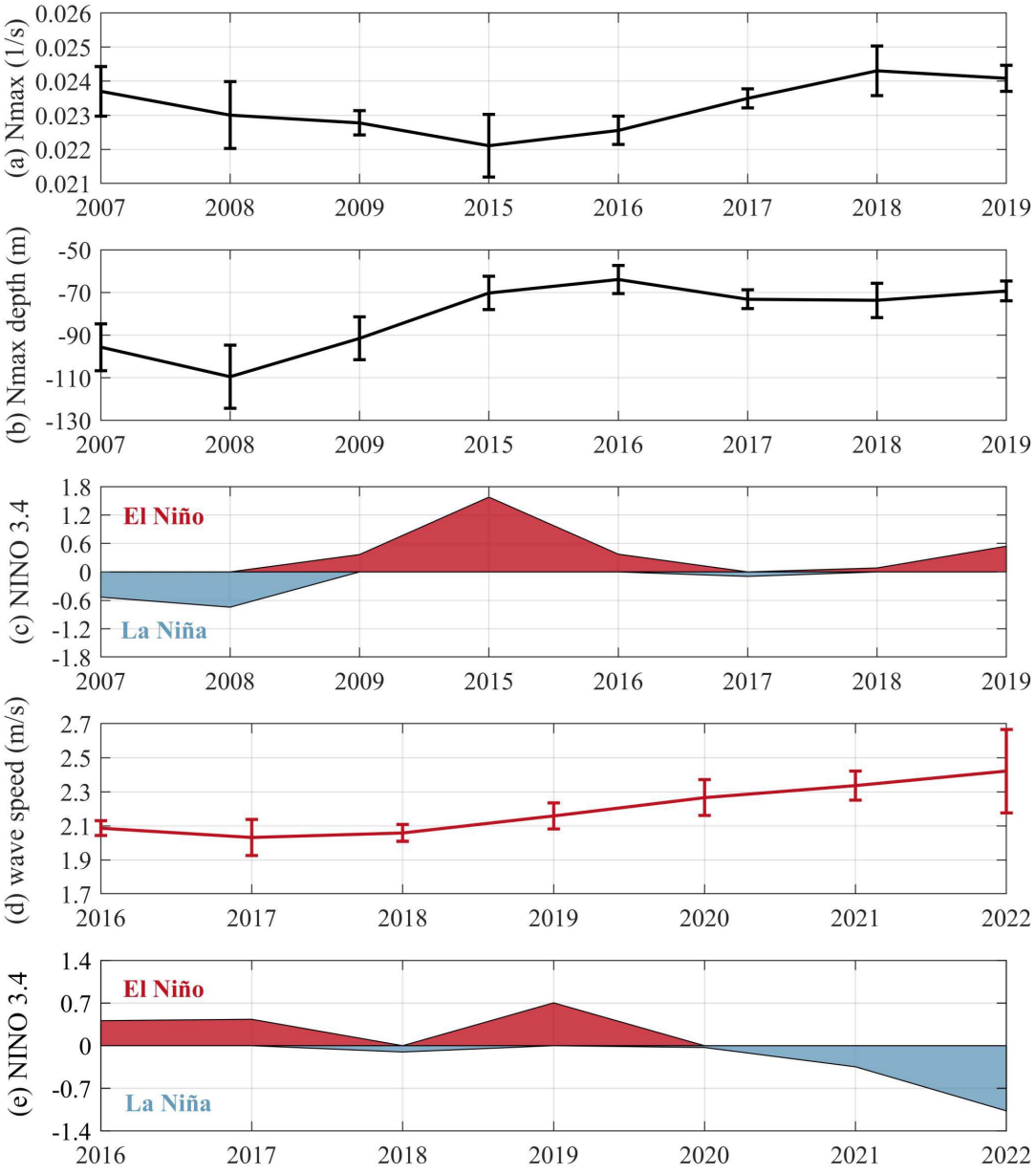


**Figure 4.** The interannual variations: the annual averages of the $N_{max}$ (a) and the $N_{maxdepth}$ (b) from Argo profiling data in the Sulu Sea and the NINO3.4 index (c) in 2007, 2008, 2009, 2015, 2016, 2017, 2018, and 2019; the averages of wave speeds (d) and the NINO3.4 index (e) in AMJ month from 2016 to 2022. The vertical bars represent ranges of one standard deviation.

## 4 Summary and Discussion

In this study, we collected 1354 groups of wave speeds in the SS from tandem satellite images with temporal intervals below 20 minutes. Based on these data, we analyzed their spatiotemporal variations and identified the potential contributing factors. The full picture of the spatial variation of wave speeds has been provided, and the multi-scale temporal variations from daily through monthly to interannual variations have also been demonstrated. Tidal current plays a significant role in modulating the daily changes of wave speeds by dominating the wave's

amplitude, while the combined effect of ocean stratification and background circulations modifies the monthly variation of wave speeds. The interannual variation of wave speeds contributed by ENSO is also found. We found that the Pearson correlation coefficient between wave speeds and the NINO3.4 index of ENSO is -0.79. The high negative correlation suggests that ISWs have a speedup in La Niña years and a slowdown in El Niño years.

We present a statistical formula for the close relationship between the wave speed and the maximum ebb tidal current speed, which has never been shown in previous studies due to the limited data volume (Apel et al., 1985; Zhao et al., 2006). The results support the study about the modulation of tidal currents on the amplitude of ISWs. However, how the tidal currents quantitatively modulate the wave amplitude needs further study.

According to the monthly averages of the wave speeds and their linear phase speeds, we found that the latter is higher than the former in October (Figure 3a), contrary to the KdV theory. Similar situations happened in previous studies (Liu et al., 2019; Tensubam et al., 2021) but were attributed to the background current that was not considered when estimating the linear phase speeds. However, our results reveal that even though the background circulation has been included, the result in October still cannot be explained by the KdV theory. Deficiencies of the KdV theory or the uncertainty of the model-derived stratification for calculating phase speeds may take this responsibility. In the future, further theoretical derivations, field measurements, and numerical simulations should be carefully designed and performed to interpret this interesting finding in October and improve the theoretical system for describing the characteristics of the ISWs.

We present for the first time a clear effect of ENSO on the wave speeds, which does not focus exclusively on the effect of ENSO on the occurrence frequency of ISWs, as in previous studies (DeCarlo et al., 2015; Chonnaniyah et al., 2021), but is more concerned with their dynamical processes. However, we have to point out that this study is restricted to a single season (spring) due to data limitations. More research on interannual variation of wave speed in different seasons are needed for verification in the future. Additionally, the same analysis can be expanded to study the interannual variations of wave speed and its relationship with ENSO in other hot spot regions, such as the SCS (Qu et al., 2004; Fang et al., 2006) and the Lombok Strait (Aiki et al., 2011), where there are strong ISWs and significant impacts from ENSO.

## Acknowledgements

This research was supported by the National Science Fund for Distinguished Young Scholars (42025605) and National Natural Science Foundation of China (42006193).

## Data Availability Statement

The AQUA MODIS images and Suomi NPP VIIRS images were downloaded from NASA (https://worldview.earthdata.nasa.gov/). HYCOM data were accessed from the Center for Ocean-Atmospheric Prediction Studies (https://www.hycom.org/dataserver). GEBCO used here was obtained from the British Oceanographic Data Center (https://www.gebco.net/). Argo profiling data were downloaded from https://www.euro-argo.eu/. The NINO3.4 index was downloaded from the University Corporation for Atmospheric Research (https://www.cgd.ucar.edu/). The TPXO tide model is available at https://www.tpxo.net/regional.

## References

Aiki, H., Matthews, J. P., & Lamb, K. G. (2011). Modeling and energetics of tidally generated wave trains in the Lombok Strait: Impact of the Indonesian Throughflow. *Journal of Geophysical Research*, 116(C3). doi:10.1029/2010jc006589

Alford, M. H., Peacock, T., MacKinnon, J. A., Nash, J. D., Buijsman, M. C., Centurioni, L. R., … (David) & Tang, T.-Y. (2015). The formation and fate of internal waves in the South China Sea. *Nature*, 521(7550), 65–69. doi:10.1038/nature14399.

Alpers, W. (1985). Theory of radar imaging of internal waves. *Nature*, 314, 245–247, doi:10.1038/314245a0

Apel, J. R., Holbrook, J. R., Liu, A. K., & Tsai, J. J. (1985). The Sulu Sea Internal Soliton Experiment. *Journal of Physical Oceanography*, 15(12), 1625–1651, doi:10.1175/1520-0485(1985)015<1625:tssise>2.0.co;25(1985)015<1613:niweit>2.0.co;2

Apel, J. R. (2002). Oceanic internal waves and solitons. *An atlas of oceanic internal solitary waves*. Global Ocean Associates, 1-40.

Apel, J. R., Ostrovsky, L. A., Stepanyants, Y. A., & Lynch, J. F. (2007). Internal solitons in the ocean and their effect on underwater sound. *The Journal of the Acoustical Society of America*, 121(2), 675-722, doi: 10.1121/1.2395914.

Cai, S., He, Y., Wang, S., & Long, X. (2009). Seasonal upper circulation in the Sulu Sea from satellite altimetry data and a numerical model. *Journal of Geophysical Research*, 114(C3), doi:10.1029/2008jc005109

Chassignet, E. P., Hurlburt, H. E., Smedstad, O.M., Halliwell, G.R., Hogan, P.J., Wallcraft, A.J.,

323 Baraille, R., Bleck, R. (2007). The HYCOM (hybrid coordinate ocean model) data
324 assimilative system. *Journal of Marine Systems*, 65, 60–83, doi: 10.1016/j.jmarsys.
325 2005.09.016.
326 Cho, C., Nam, S. H., & Song, H. C. (2016). Seasonal variation of speed and width from
327 kinematic parameters of mode-1 nonlinear internal waves in the northern East China Sea.
328 *Journal of Geophysical Research: Oceans*, 121(8), 5942-5958, doi:10.1002/2016JC012035
329 Chonnaniyah, Osawa, T., Wayan Gede Astawa Karang, I., & As-syakur, A.R. (2021). Variability
330 of Internal Solitary Waves Detection in the Lombok Strait Observed by Sentinel-1 SAR: The
331 Role of Monsoon, IOD, and ENSO. 2021 7th Asia-Pacific Conference on Synthetic Aperture
332 Radar (APSAR), 1-5.
333 Da Silva, J., Ermakov, S., Robinson, I., Jeans, D., Kijashko, S., (1998). Role of surface films in
334 ERS SAR signatures of internal waves on the shelf: 1. Short-period internal waves. *Journal of*
335 *Geophysical Research: Oceans*, 103, 8009–8031.
336 Da Silva, J. C. B. (2002). On the observability of internal tidal waves in remotely-sensed ocean
337 colour data. *Geophysical Research Letters*, 29(12). doi:10.1029/2001gl013888.
338 DeCarlo, T. M., Karnauskas, K. B., Davis, K. A., & Wong, G. T. F. (2015). Climate modulates
339 internal wave activity in the Northern South China Sea. *Geophysical Research Letters*, 42(3),
340 831–838, doi:10.1002/2014gl062522
341 Egbert, G. D., & Erofeeva, S.Y. (2002). Efficient inverse modeling of barotropic ocean tides.
342 *Journal of Atmospheric and Oceanic technology*, 19, 183–204.
343 Emberson, R., Kirschbaum, D., & Stanley, T. (2021). Global connections between El Nino and
344 landslide impacts. *Nature Communications*, 12(1), doi:10.1038/s41467-021-22398-4

345 Fang, W. D., Guo, J. J., Shi, P., & Mao, Q. W. (2006). Low frequency variability of South China
346 Sea surface circulation from 11 years of satellite altimeter data. *Geophysical Research Letters*,
347 33(22), doi: 10.1029/2006GL027431.
348 Garrett, C. (2003). Internal tides and ocean mixing. *Science*, 301(5641), 1858-1859,
349 doi:10.1126/science.1090002
350 GEBCO Compilation Group. (2022). GEBCO_2022 Grid. doi:10.5285/e0f0bb80-ab44-2739-
351 e053-6c86abc0289c.
352 Giese, G. S., Chapman, D. C., Collins, M. G., Encarnacion, R., & Jacinto, G. (1998). The
353 Coupling between Harbor Seiches at Palawan Island and Sulu Sea Internal Solitons. *Journal of*
354 *Physical Oceanography*, 28(12), 2418–2426. doi:10.1175/1520-
355 0485(1998)028<2418:tcbhsa>2.0.co;2
356 Gill, A. E. (1982). International Geophysics. *Atmosphere-Ocean Dynamics*. Amsterdam. The
357 Netherlands: Elsevier.
358 Han, W. Q., Moore, A. M., Levin, J., Zhang, B., Arango, H. G., Curchitser, E., Lorenzo, E. D.,
359 Gordon, A. L., & Lin, J. L. (2009). Seasonal surface ocean circulation and dynamics in the
360 Philippine Archipelago region during 2004-2008. *Dynamics of Atmospheres and Oceans*,
361 47(1-3), 114-137, doi:10.1016/j.dynatmoce.2008.10.007
362 Haury, L. R., Briscoe, M. G., & Orr, M. H. (1979). Tidally generated internal wave packets in
363 Massachusetts Bay. *Nature*, 278(5702), 312–317. doi:10.1038/278312a0.
364 Huang, X. D., Zhang, Z. W., Zhang, X. J., Qian, H. B., Zhao, W., & Tian, J. W. (2017). Impacts
365 of a Mesoscale Eddy Pair on Internal Solitary Waves in the Northern South China Sea
366 revealed by Mooring Array Observations. *Journal of Physical Oceanography*, 47(7), 1539-
367 1554, doi: 0.1175/JPO-D-16-0111.1.

368 Jackson, C. R. (2004). An Atlas of internal solitary-like waves and their properties, 2nd ed.,
369 Global Ocean Associates, Washington, D. C. [Available at
370 http://www.internalwaveatlas.com/Atlas2index.html]
371 Jackson, C., (2007). Internal wave detection using the moderate resolution imaging
372 spectroradiometer (MODIS). *Journal of Geophysical Research: Oceans*, 112.
373 Jackson, C. R. (2009). An empirical model for estimating the geographic location of nonlinear
374 internal solitary waves. *Journal of Atmospheric and Oceanic Technology*, 26(10), 2243-2255,
375 doi:10.1175/2009JTECHO638.1
376 Jackson, C., Arvelyna, Y., & Asanuma, I. (2011). High-Frequency Nonlinear Internal Waves
377 Around the Philippines. *Oceanography*, 24(01), 90–99. doi:10.5670/oceanog.2011.06.
378 Klein, S. A., Soden, B. J., Lau, N. C. (1999). Remote Sea Surface Temperature Variations during
379 ENSO: Evidence for a Tropical Atmospheric Bridge. *Journal of Climate*, 12(4), 917–932.
380 doi:10.1175/1520-0442(1999)012<0917:rsstvd>2.0.co;2.
381 Li, X. P., Clemente-Colon, P., & Friedman, K. (2000). Estimating oceanic mixed layer depth
382 from internal wave evolution observed from RADARSAT-1 SAR. *Johns Hopkins Apl*
383 *Technical Digest*, 21(1), 130-135.
384 Lien, R. C., D'Asaro, E. A., Henyey, F. S., Chang, M. H., Tang, T. Y., & Yang, Y. J. (2012).
385 Trapped core formation within a shoaling nonlinear internal wave. *Journal of Physical*
386 *Oceanography*, 42, 511-525, doi: 10.1175/2011JPO4578.1.
387 Lindsey, D. T., Nam, S. H., & Miller, S. D. (2018). Tracking oceanic nonlinear internal waves in
388 the Indonesian seas from geostationary orbit. Remote Sensing of Environment, 208, 202-209,
389 doi: 10.1016/j.rse.2018.02.018.

390 Liu, A. K., Holbrook, J. R., & Apel, J. R. (1985). Nonlinear Internal Wave Evolution in the Sulu
391 Sea. *Journal of Physical Oceanography*, 15(12), 1613–1624, doi:10.1175/1520-
392 0485(1985)015<1613:NIWEIT>2.0.CO;2
393 Liu, A. K., Ramp, S. R., Zhao, Y., & Tang, T. Y. (2004). A case study of internal solitary wave
394 propagation during ASIAEX 2001, *IEEE Journal of Oceanic Engineering*, 29(4), 1144-1156,
395 doi:10.1109/JOE.2004.841392.
396 Liu, B., Yang, H., Zhao, Z., & Li, X. (2014). Internal solitary wave propagation observed by
397 tandem satellites. *Geophysical Research Letters*, 41(6), 2077–2085,
398 doi:10.1002/2014gl059281.
399 Liu, B., & D'Sa, E. J. (2019). Oceanic Internal Waves in the Sulu-Celebes Sea Under Sunglint
400 and Moonglint. *IEEE Transactions on Geoscience and Remote Sensing*, 1–11,
401 doi:10.1109/tgrs.2019.2904402.
402 Lynch, J. F., Lin, Y. T, Duda, T. F., & Newhall, A. E. (2010). Acoustic ducting, reflection,
403 refraction, and dispersion by curved nonlinear internal waves in shallow water. *IEEE Journal*
404 *of Oceanic Engineering*, 35, 12-27.
405 MacKinnon, J. A., Zhao, Z., Whalen, C. B., Waterhouse, A. F., Trossman, D. S., Sun, O. M., …
406 & Alford, M. H. (2017). Climate Process Team on Internal Wave–Driven Ocean Mixing.
407 Bulletin of the American Meteorological Society, 98(11), 2429–2454, doi:10.1175/bams-d-16-
408 0030.1.
409 Osborne, A., Burch, T., & Scarlet, R. (1978). The influence of internal waves on deep-water
410 drilling. *Journal of Petroleum Technology*, 30, 1497-1504, doi.org/10.2118/6913-PA.

411 Porter, D. J., & Thompson, D. R. (1999). Continental shelf parameters inferred from SAR
412 internal wave observations. *Journal of Atmospheric and Oceanic Technology*, 16(4), 475-487,
413 doi:10.1175/1520-0426(1999)016<0475:CSPIFS>2.0.CO;2.
414 Qu, T., Kim, Y. Y., Yaremchuk, M., Tozuka, T., Ishida, A., & Yamagata, T. (2004). Can Luzon
415 Strait Transport Play a Role in Conveying the Impact of ENSO to the South China Sea?
416 *Journal of Climate*, 17(18), 3644–3657. doi:10.1175/1520
417 0442(2004)017<3644:clstpa>2.0.co;2
418 Ramp, S. R., Yang, Y. J. Yang, & Bahr, F. L. Bahr (2010). Characterizing the nonlinear internal
419 wave climate in the northeastern South China Sea. *Nonlinear Processes in Geophysics*, 17(5),
420 481–498, doi:10.5194/npg-17-481-2010.
421 Tensubam, C. M., Raju, N. J., Dash, M. K., & Barskar, H. (2021). Estimation of internal solitary
422 wave propagation speed in the Andaman Sea using multi–satellite images. *Remote Sensing of*
423 *Environment*, 252, 112123, doi:10.1016/j.rse.2020.112123.
424 Trenberth, K. E., & Stepaniak, D. P. (2001). Indices of El Nino Evolution, *Journal of Climate*,
425 14(8), 1697-1701, doi: 10.1175/1520-0442(2001)014<1697:LIOENO>2.0.CO;2.
426 Wang, Y. H., Dai, C. F., & Chen, Y. Y. (2007). Physical and ecological processes of internal
427 waves on an isolated reef ecosystem in the South China Sea, *Geophysical Research Letters*, 34,
428 L18609, doi:10.1029/2007GL030658.
429 Wang, C., & Pawlowicz, R. (2011). Propagation speeds of strongly nonlinear near-surface
430 internal waves in the Strait of Georgia, *Journal of Geophysical Research*, 116(C10), doi:
431 116(C10). doi:10.1029/2010jc006776.

Wang, T. X., Huang, X. D., Zhao, W., Zheng, S. H., Yang, Y.C., & Tian, J. W. (2022). Internal solitary wave activities near the Indonesian submarine wreck site inferred from satellite images, *Journal of Marine Science and Engineering*, 10(2), 197, doi: 10.3390/jmse10020197.

Zhang, X. D., & Li, X. F. (2022). Satellite data-driven and knowledge-informed machine learning model for estimating global internal solitary wave speed. *Remote Sensing of Environment*, 283, 113328, doi: 10.1016/j.rse.2022.113328.

Zheng, X. H., & Klemas, V. (1993). Statistical and dynamical analysis of internal waves on the continental shelf of the middle Atlantic bight from space shuttle photographs, *Journal of Geophysical Research*, 98(C5), 8495-8504, doi: 10.1029/92jc02955.

Zhao, Z. X., & Alford, M. H. (2006), Source and propagation of internal solitary waves in the northeastern South China Sea. *Journal of Geophysical Research: Oceans*, 111(11), doi:10.1029/2006JC003644.

Zhou, J. X., Zhang, X. Z., & Rogers, P. H. (1991). Resonant interaction of sound wave with internal solitons in the coastal zone. *The Journal of the Acoustical Society of America*, 90(4), doi: 10.1121/1.401632.